

Multi-domain analytical rotor model with buried permanent magnets in V-arrangement for high-speed applications

MAXIMILIAN LAUERBURG  , POLKRIT TORAKTRAKUL, KAY HAMEYER

*Institute of Electrical Machines (IEM), RWTH Aachen University
Schinkelstr. 4, D-52062 Aachen, Germany*

e-mail: {  maximilian.lauerburg/hameyer@iem.rwth-aachen.de, polkrit.toraktrakul@rwth-aachen.de }

(Received: 06.01.2023, revised: 29.03.2023)

Abstract: Different buried permanent magnet arrangements in rotors are compared based on electrical machines found in literature regarding high-speed capability. An analytical approach is presented to analytically calculate mechanical stresses in the bilateral and central bridge of V arrangements in order to determine the achievable circumferential velocity of a rotor geometry. The mechanical model is coupled to an analytical model which can determine the flux density in the main air gap under consideration of flux leakage within the rotor. The multi-domain model enables the analytical design of high-speed rotors with buried permanent magnets in V-arrangement.

Key words: analytical calculation method, arrangement of buried permanent magnets, high-speed rotor morphology, multi-domain design process

1. Overview of synchronous machines with buried permanent magnets with regard to high-speed capability

High-speed operation is desirable especially in mobile applications due to a potentially larger achievable power density of the electrical machine [1]. The required torque at constant power output is lowered by increasing the rotational speed. Therefore, the dimensions of the electrical machine are reduced. There can be noticed a trend for high-speed operation in recent years of automotive electrification and servo motor drives [2]. A machine with buried permanent magnets for automotive application with a maximum rotational speed of 20 000 rpm and a gravimetric power density of 15.6 kW/kg is produced in series by LUCID Motors [3].



© 2023. The Author(s). This is an open-access article distributed under the terms of the Creative Commons Attribution-NonCommercial-NoDerivatives License (CC BY-NC-ND 4.0, <https://creativecommons.org/licenses/by-nc-nd/4.0/>), which permits use, distribution, and reproduction in any medium, provided that the Article is properly cited, the use is non-commercial, and no modifications or adaptations are made.

However, the term high-speed is not referring to the rotational speed n , it mainly relates to the maximum circumferential velocity at the rotor outer diameter r_{rotor} . The circumferential velocity sets the radial dimensions of the rotor in relation to the rotational speed and therefore directly correlates to the mechanical strength of the rotor. According to [1], the tangential stresses σ_t within the rotor are proportional to the square of the circumferential velocity v_p , Eq. (1).

$$v_p = 2\pi n r_{\text{rotor}} \sim \sqrt{\sigma_t}. \quad (1)$$

Interior permanent magnet synchronous machines (IPMSMs) are mainly used as traction machines in current automotive industry [2]. In contrast to surface permanent magnets (SPMSM), buried permanent magnets can be arranged within the rotor such that rotor saliency is achieved. IPMSMs enable additional reluctance torque at constant current compared to SPMSMs. The lamination sheets secure the permanent magnets against centrifugal forces in IPMSMs. A retaining sleeve and therefore an additional component as well as manufacturing process is required for rotor integrity in SPMSMs.

An overview of different rotor topologies with buried permanent magnets is given in Fig. 1. The permanent magnets can either be arranged radially such as spokes, tangentially to the outer contour or in a V-shape. T-arrangement and V-arrangement can be combined to a Δ -shape.

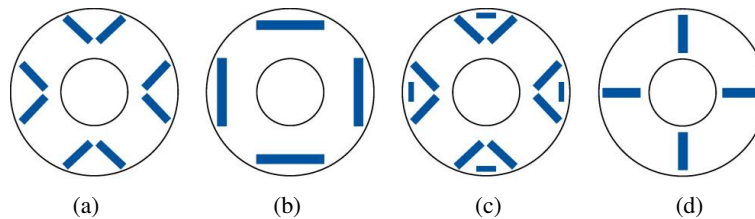


Fig. 1. Overview to arrange permanent magnets within rotors of electrical machines; (a) V-arrangement; (b) T-arrangement; (c) Δ -arrangement and (d) Spoke-arrangement

Changing the position of permanent magnets within the rotor affects electromagnetics and mechanics. The rotor topologies are ranked in Table 1 based on comparisons done in [4–7]. The Spoke-arrangement performs worst, due to the fact that flux leakage within the rotor has the tendency to be comparatively large and therefore the efficiency is low. Additionally, the Spoke-arrangement tend to have a lower rotor strength. The V-, T- and Δ -arrangement have a much better rotor saliency and therefore the efficiency is higher. The difference in power density is mainly due to different rotor strength which affects the achievable circumferential velocity.

Table 1. Comparison of permanent magnet arrangements [4–7]

	V	T	Δ	Spoke
Power density	++	+	0	–
Rotor strength	+	++	0	–
Rotor saliency	+	0	++	–
Efficiency	+	0	++	–

Therefore, only the V-, T- and Δ -arrangement are analyzed further. These topologies are compared based on state-of-the-art machine designs published in [2] and [8–22], which are either used in series production or have been studied in a research context on test benches (Fig. 2).

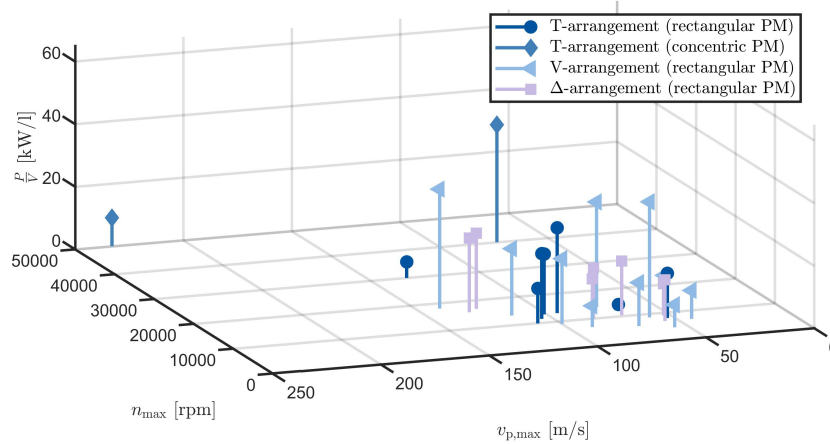


Fig. 2. Influence of permanent magnet arrangement on high-speed capability based on machine designs found in [2] and [8–22]

Only rectangular shaped permanent magnets are used for the compared V- and Δ -arrangements. The T-arrangement is distinguished between permanent magnets with a rectangular and a concentric shape. It can be noticed that for IPMSM designs which are using rectangular shaped permanent magnets a circumferential velocity higher than 150 m/s cannot be achieved with current lamination sheets.

The largest circumferential velocity with rectangular permanent magnets is achieved by the traction machine used in the Tesla Model 3 which has a V-arrangement and achieves a circumferential velocity of 140 m/s at 18 000 rpm [2]. However, a machine designed in scientific context with a T-arrangement achieves a significantly larger rotational speed of 30 000 rpm [19]. Achievable rotational speeds of T-arrangement have the tendency to be larger than the other two configurations as the maximum mechanically allowable rotor diameter reduces with increasing rotational speeds and less space within the rotor is needed to arrange the permanent magnets tangentially rather than in a V- or Δ -shape. The achievable circumferential velocity of the Δ -arrangement is the lowest due to the fact that comparatively more cavities are required and therefore the notch effect becomes higher.

The largest circumferential velocity of 234 m/s at a rotational speed of 50 000 rpm is achieved by a motor with a T-arrangement published in [9]. The authors suggest the use of concentric shaped permanent magnets in order to distribute mechanical stresses in the rotor more evenly. The rotor strength is increased drastically as a result. The rotor cross-section has some similarity to an SPMSM rotor however the outer sleeve structure is connected via bridges with the inner part of the rotor iron. A synchronous machine using concentric permanent magnets for high-speed spindle applications is discussed in [15]. The rotor achieves a rotational speed of 40 000 rpm

with a comparatively low circumferential velocity of 74 m/s due to the small rotor diameter electromagnetically required for the application.

The basic motivation for high-speed operation to maximize power density with large rotational speeds is proven by the trend of the compared machine designs. The maximum of power density is achieved with the largest rotational speed. In comparison, the V-arrangement performs best in terms of mechanical and electromagnetic performance. Therefore, an analytical design morphology for rotors in synchronous machines with permanent magnets in V-arrangement (V-IPMSM) will be derived in the following.

2. Analytical model to calculate mechanical stresses in magnet bridges of rotors with permanent magnets in V-arrangement

Mechanical integrity of the rotor has to be ensured during the design process of high-speed electrical machines in order to guarantee safe operation. The Equivalent Ring Method (ERM) was introduced in [23] in order to analytically calculate mechanical stresses in magnet bridges of tangentially arranged magnet pockets, so the maximum achievable rotational speed of a given rotor cross-section can be determined without the FEA.

The outer holding band (OHB) of a rotor is the ring structure bordered by the rotor outer contour and the most adjacent cavity, such as a magnetic pocket [24]. The OHB determines the dimensions of the equivalent ring, which is used for analytical calculation. The equivalent arrangement is assigned with an equivalent density according to the materials used in the rotor. The notch effect due to different radii and bridge thicknesses was assumed to be constant in [23].

Attempts have been published in [7] and [25] to apply this method for V-arrangements under consideration of the angle between the permanent magnets Θ within one pole. However, the published methods were relatively inaccurate in determining mechanical stresses in the central magnet bridge compared to FEA. For this reason, a new model is presented.

The respected areas in the rotor cross-section have to be determined at first (Fig. 3). A_{Fe} is the area of the lamination sheet which loads the bilateral bridges as well as the central bridge. A_{PM} is the total area of permanent magnets within one pole. A_{equiv} is the area of the equivalent ring where the radius of the inner contour of the ring $r_{i,equiv}$ is given by Eq. (2).

$$r_{i,equiv} = r_{rotor} - h_b. \quad (2)$$

h_b is the thickness of the bilateral bridge and r_{rotor} is the rotor radius. The thickness of the OHB is equal to the thickness of the bilateral bridges. The equivalent ring is assigned with an equivalent density ρ_{equiv} , Eq. (3).

$$\rho_{equiv} = \frac{\rho_{Fe} + \rho_{PM}}{2} \cdot \frac{A_{Fe} + A_{PM}}{A_{equiv}}. \quad (3)$$

ρ_{Fe} is the density of the lamination sheet material and ρ_{PM} the density of the material used for the permanent magnets. The nominal mechanical stress σ_{equiv} in the magnet bridges at a defined rotational speed n can be determined with (4).

The V-arrangement moves towards the inside of the rotor with increasing thickness of the bilateral magnet bridges and thus the thickness of the OHB increases, which leads to a reduction

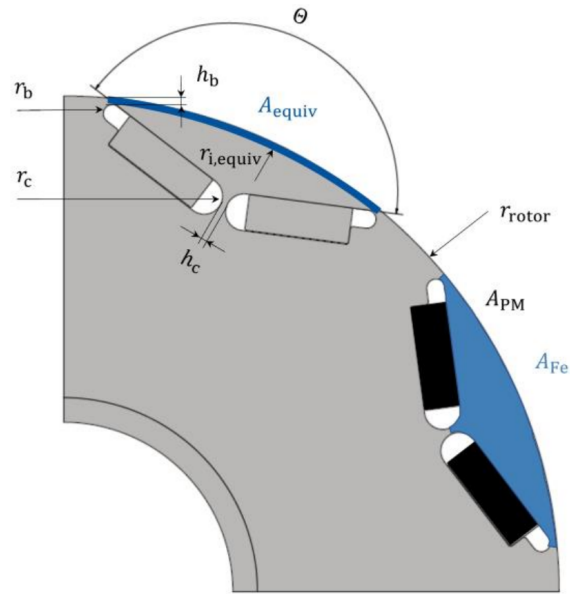


Fig. 3. Dimensions and respected areas for ERM of V-arrangement

in the mechanical stress.

$$\sigma_{equiv} = \left(\frac{r_a + r_{i,equiv}}{2} \right)^2 \cdot (2\pi n)^2 \cdot \rho_{equiv}. \quad (4)$$

The maximum mechanical stress σ_{max} due to the notch effect of the magnet pocket can be evaluated with the stress concentration factor K_t , Eq. (5). The presented stress concentration factors are a modification of factors shown in [26].

$$\sigma_{max} = K_t \cdot \sigma_{equiv}. \quad (5)$$

The stress concentration factor $K_{t,bilateral}$ for the bilateral bridges is given by Eq. (6). r_b is the radius of the magnet pocket facing the OHB.

$$K_{t,bilateral} = \frac{\frac{2}{\sqrt{7}} \cdot 10.8 \sqrt{\frac{h_b}{r_b}} \cdot 85 \sqrt{\frac{h_c}{r_c}} \cdot \sqrt{\frac{h_b}{h_c}} \cdot \left(\frac{h_b}{r_b} + 1 \right) \cdot \sqrt{\frac{h_b}{r_b}}}{\left(\frac{h_b}{r_b} + 1 \right) \cdot \tan^{-1} \left(\sqrt{\frac{h_b}{r_b}} \right) + \sqrt{\frac{h_b}{r_b}}} \cdot \cos \left(\frac{1}{\sqrt[3]{3.95}} \cdot \left(\Theta - \frac{2\pi}{3} \right) \right). \quad (6)$$

The stress concentration factor $K_{t,central}$ for the central bridge is given by Eq. (7). h_c is equal to the thickness of the central bridge and r_c is the adjacent radius of the magnet pocket contour.

$$K_{t,central} = \left(\sqrt{\frac{78}{12}} \cdot \left(\frac{3 \cdot h_c}{3 \cdot h_c + r_c} \right)^{2 \cdot \sqrt{97.3}} + \frac{3}{\sqrt{37}} \cdot \left(\frac{3 \cdot h_c + r_c}{3 \cdot h_c} \right)^{\frac{2}{\sqrt{97}}} \right) \cdot \left(\frac{h_b}{h_c} \right)^{\frac{2}{\sqrt{10}}} \cos \left(\frac{1}{\sqrt[3]{3.95}} \cdot \left(\Theta - \frac{2\pi}{3} \right) \right). \quad (7)$$

The achievable circumferential velocity under consideration of a safety factor S can be determined with Eq. (8).

$$v_p = \sqrt{\frac{\frac{R_p}{S}}{K_t \cdot \left(\frac{r_a + r_{i,equiv}}{2r_a}\right)^2 \cdot \rho_{equiv}}} \tag{8}$$

The safety factor determines how close the local mechanical stress σ_{xyz} within the rotor is to the yield strength R_p of the electrical sheet at maximum rotor speed, Eq. (9). Thus, the safety factor represents the mechanical utilization of the rotor materials.

$$S = \frac{R_p}{\sigma_{xyz}} \tag{9}$$

The maximum achievable circumferential velocity $v_{p,max}$ is reached when the mechanical stress in one of the magnet bridges reaches the yield strength R_p of the lamination sheet. In this case, the safety factor is equal to 1.

Equation (8) has to be evaluated for the bilateral bridge with $K_{t,bilateral}$ and for the central bridge with $K_{t,central}$. The technically usable circumferential velocity $v_{p,max}$ is the minimum of the bridge related terms, Eq. (10).

Figure 4 displays the determination of the technically usable circumferential velocity $v_{p,max}$, being the minimum of both surfaces $v_{p,bilateral}$ and $v_{p,central}$. The achievable circumferential velocity increases with larger bridge thicknesses in general. However, the bilateral bridge tend to be the bottleneck at equal bridge thickness and radii.

$$v_{p,max} = \min(v_{p,bilateral}, v_{p,central}) \tag{10}$$

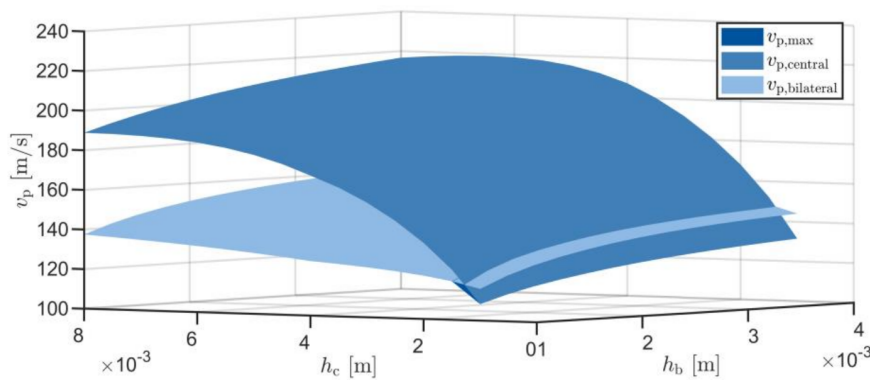


Fig. 4. Bridge related achievable circumferential velocity and technical usable circumferential velocity in relation to bridge thicknesses. The safety factor is equal to 1 so the mechanical stresses reach the materials yield strength

The model is validated based on mechanical simulations in ANSYS. The contact definition between rotor components and material parameters are taken from [27], where mechanical simulations show good agreement with rotor deformation measurements performed under rotational

speed as well as burst test for a high-speed PMSM rotor. The contact modeling between rotor components and material parameters presented in [27] is adopted for the own simulations.

An exemplary von Mises stress distribution in the lamination sheet at a rotational speed is shown in Fig. 5(b). The stresses in the bilateral and central magnet bridges are limiting the high-speed operation. Mechanical stresses due to the press-fit between lamination and shaft are prominent in the central part of the rotor. The comparison between the analytical model and the FEA is shown in Fig. 5(a). The new model displays minor deviations from the simulation.

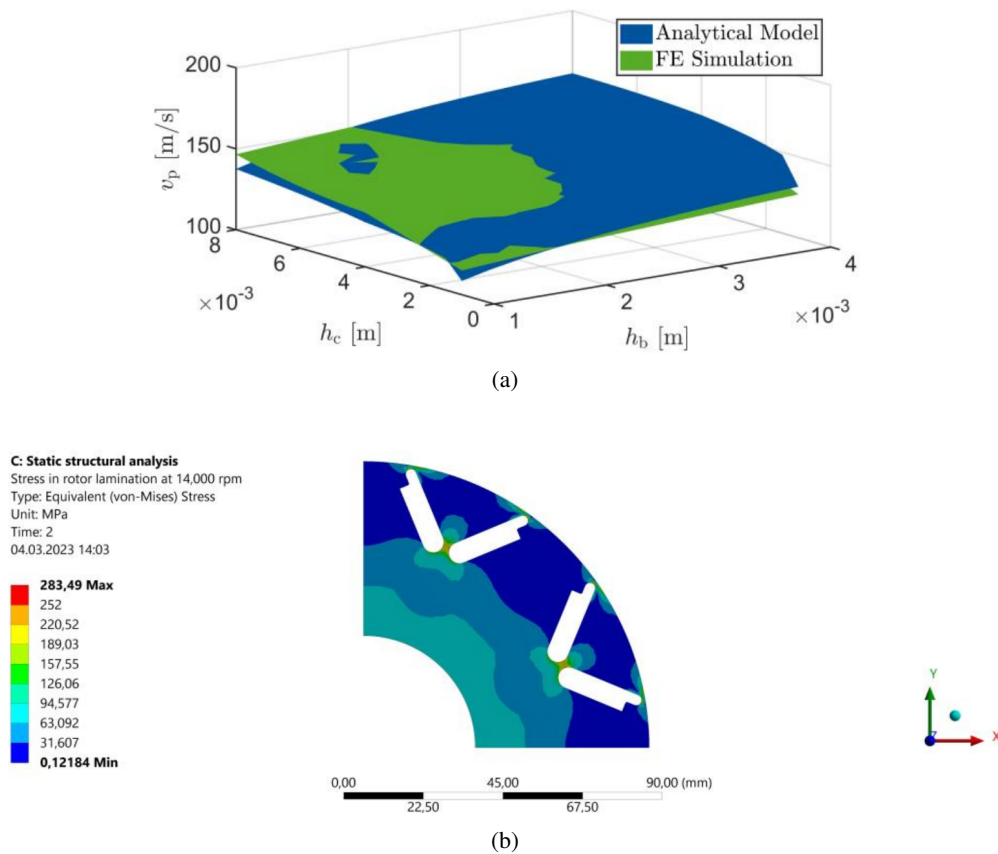


Fig. 5. (a) Comparison between analytical model and FE Simulation in ANSYS with respect to maximum achievable circumferential velocity ($S = 1$); (b) exemplary von Mises stress distribution in lamination sheet

The presented analytical model shows that large bridge thicknesses are favorable in order to maximize rotor strength. However, large bridge thicknesses lead to increased flux leakage which reduces the machine performance. The optimum bridge thickness is a tradeoff between mechanical and electromagnetic boundary conditions [28]. Therefore, the presented mechanical model is now coupled with electromagnetics.

3. Coupling of mechanical model with electromagnetic and thermal constraints

At first, the mechanical model is extended by electromagnetic boundary conditions. For a given bridge dimension, the stray flux and thus the utilization of the buried permanent magnets can be determined. Here, an approach is presented to take temperature dependencies into account.

3.1. Analytical model to calculate air gap flux density for V-arrangement

Buried permanent magnets are secured against centrifugal forces by the lamination sheets, in particular the magnet bridges. The magnetic flux imposed by the permanent magnets prefers the path with the lowest magnetic resistance.

Due to the proximity of the magnet bridges to the permanent magnet, the magnetic flux has the opportunity to close already in the rotor and thus not contribute to the flux linkage to the stator (Fig. 6). As a result, more input current is required for torque generation and efficiency decreases.

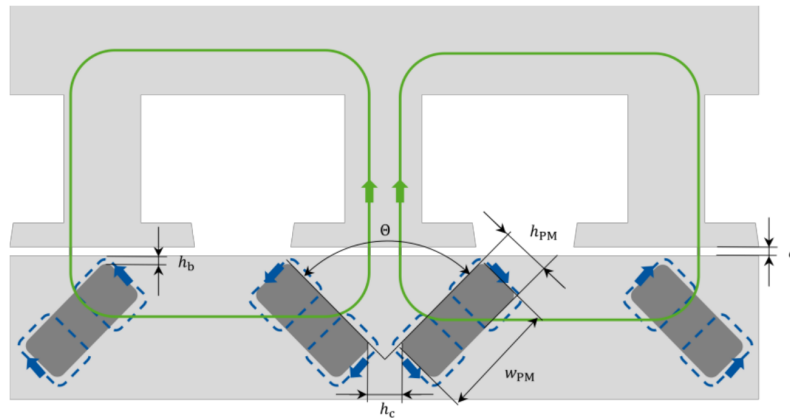


Fig. 6. Flux leakage within rotor with buried permanent magnets (dashed lines); only the magnetic flux going from the rotor into the stator contributes to the electromagnetic energy conversion (continuous lines)

With increasing bridge thickness, the saturation of the electrical steel in this area decreases and thus the magnetic resistance decreases. Coupling the mechanical model with an electromagnetic model which considers the flux leakage for defined magnet bridge dimensions would allow a multi-domain analytical design.

The presented model is an extension of the analytical model presented in [29] for the use of an SPMSM. In the new model, the angle between the permanent magnets as well as the dimensions of the magnetic bridges are considered.

The magnetic resistance of the main air gap R_δ in the machine is considered with Eq. (11). δ is equal to the height of the air gap, r_δ the average air gap radius, l_{Fe} the axial length of the lamination stack, μ_0 the vacuum permeability and p the pole pair number.

$$R_\delta = \frac{\delta}{\mu_0 \frac{2\pi r_\delta l_{Fe}}{p}} \quad (11)$$

The magnetic resistance of the permanent magnet R_{PM} can be calculated with Eq. (12). h_{PM} is the height of the permanent magnet, w_{PM} its width and the axial length of the permanent magnets is assumed to be equal to the axial length of the lamination sheet l_{Fe}

$$R_{PM} = \frac{h_{PM}}{\mu_0 w_{PM} l_{Fe}}. \quad (12)$$

It is assumed that the magnetization within the magnetic bridge is homogeneous so the bridges can be seen as a bar structure within the rotor with an equivalent magnetic resistance.

The magnetic resistance of the bilateral bridge R_b can be determined with Eq. (13). l_b is equal to the length of the bilateral bridge with constant magnetization and μ_r the relative permeability of the bilateral bridge. The relative permeability of the magnet bridge is dependent on the operation of the electrical machine.

$$R_b = \frac{l_b}{\mu_r \mu_0 h_b l_{Fe}}. \quad (13)$$

The magnetic resistance of the central bridge can be calculated with e.g. (14). Also here, l_c is the length of the central bridge at constant flux density and μ_r its relative permeability.

$$R_c = \frac{l_c}{\mu_r \mu_0 h_c l_{Fe}}. \quad (14)$$

The flux density in the air gap B_δ can be determined with Eq. (15). B_R is the remanence flux density and H_C is the coercive field strength of the permanent magnets used.

$$B_\delta = \frac{B_R}{1 + \frac{R_\delta}{R_{PM}} \frac{\mu_M}{\mu_0} \cdot \frac{14}{\pi^8} \cdot \cosh\left(\frac{3\pi}{2}\Theta - \pi\right) + 2\pi^8 \frac{R_\delta^2}{R_c R_b}}. \quad (15)$$

The remanence flux density is reduced by the dimensions within the magnetic circuit. Hence, the air gap flux density can never be as large as the remanence flux density. Figure 7(a) is showing good agreement between the analytical model and the FE Simulation. An exemplary flux density distribution in the respected machine is given in Fig. 7(b). Changing the angle

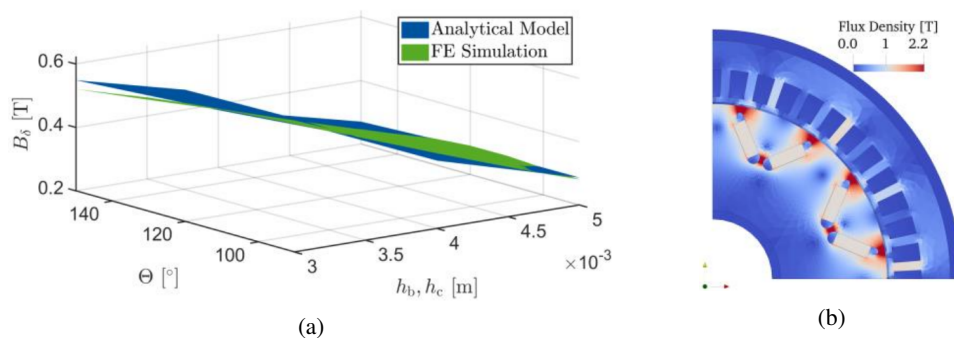


Fig. 7. (a) Comparison between analytical model and FE Simulation with respect to air gap flux density; (b) exemplary flux density distribution in respected machine

between the permanent magnets at constant bridge thicknesses influences the burial depth of the permanent magnets. Thus, the angle affects the air gap flux density. The coupling of mechanical and electromagnetic model enables the simultaneous assessment of rotor strength and flux linkage to the stator for given bridge thicknesses (Fig. 8).

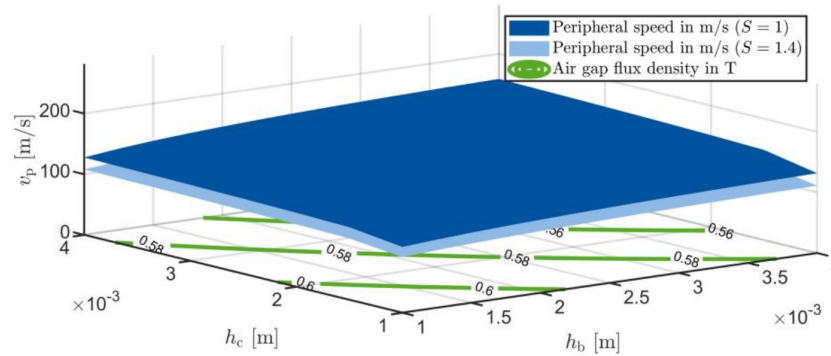


Fig. 8. Influence of safety factor on achievable circumferential velocity and allocation to air gap flux density in relation to bridge thicknesses

3.2. Consideration of temperatures in presented model

The yield strength R_p of steels usually decreases with increasing temperatures. This temperature dependence can be considered by the analytical model presented in [30]. The demagnetization behavior of permanent magnets is also temperature-dependent. Accordingly, the temperature changes B_R and H_C . Information on demagnetization behavior can be obtained from the data sheets provided by the manufacturers. A semi-physical model to determine the demagnetization curve for a specific temperature based on measurements performed at other temperatures is presented in [31].

3.3. Discussion of multi-domain model in the context of machine design

The design of a rotor can be driven by different requirements. This can be, for example, a required maximum rotational speed in the case of a direct drive, as in compressors. Available installation space and weight constraints can motivate high-speed operation in the case of indirect drives.

The mechanical design of the rotor is based on a desired safety factor. The safety factor influences not only the extent to which the material is mechanically utilized, but also the accumulation of material damage over the number of operating cycles. Material fatigue generally decreases as the safety factor increases which would favor large bridge thicknesses [32].

The extent to which large bridge thicknesses lead to electromagnetic drawbacks at constant permanent magnet dimensions depends on the operating strategy in the machine map (Fig. 9). For operating points in the base speed range, it is advantageous to have the lowest possible leakage flux in order to minimize the current requirement for torque generation. For operating points in the field weakening range, however, higher leakage fluxes are acceptable due to the fact

that less additional current is required for field weakening. However, if an electrical machine is frequently operated in field weakening range, it is preferable to reduce the permanent magnet volume rather than to reduce the utilization of the permanent magnets by increasing the bridge thickness. The interaction between required permanent magnet volumes and bridge thicknesses must be evaluated and adjusted in the context of an operating cycle.

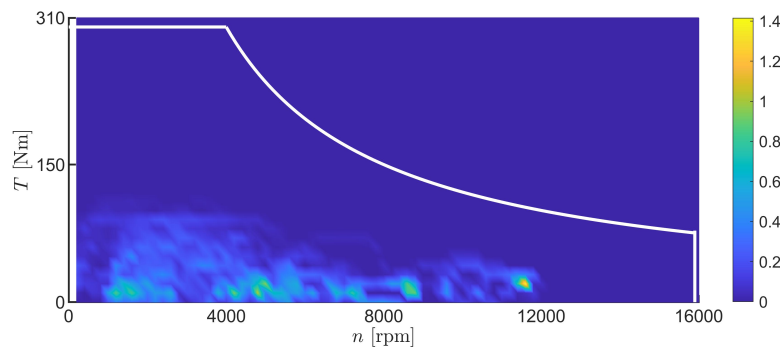


Fig. 9. Exemplary relative frequency distribution in % of operating points in the torque-speed map of an full electric vehicle during WLTP; the map limit is shown in white

4. Conclusions

Different arrangements of buried permanent magnets in rotors of synchronous machines are compared to each other in terms of high-speed capability. The T-arrangement exhibits the largest rotor strength. The V-arrangement represents a good compromise between electromagnetic and mechanical requirements.

A multi-domain model for the analytical design of magnet bridges for rotors with buried permanent magnets in a V-arrangement is shown. It is possible to consider mechanics, electromagnetics as well as thermal constraints. Burst tests to further validate the mechanical model for rotors with buried permanent magnets in V-arrangement are reasonable.

References

- [1] Binder A., Schneider T., *High-Speed Inverter-Fed AC Drives*, in International Aegean Conference on Electrical Machines and Power Electronics, IEEE (2007), DOI: [10.1109/ACEMP.2007.4510476](https://doi.org/10.1109/ACEMP.2007.4510476).
- [2] Krings A., Monissen C., *Review and Trends in Electric Traction Motors for Battery Electric and Hybrid Vehicles*, in International Conference on Electrical Machines, IEEE (2020), DOI: [10.1109/ICEM49940.2020.9270946](https://doi.org/10.1109/ICEM49940.2020.9270946).
- [3] <https://www.lucidinsider.com/2022/09/13/lucid-motors-tech-talk-on-drive-unit-motor/>, accessed February 2023.
- [4] Liu C., Chen H., Zhao J., Belahcen A., *Research on the Performances and Parameters of Interior PMSM Used for Electric Vehicles*, in Transactions on Industrial Electronics, IEEE (2016), DOI: [10.1109/TIE.2016.2524415](https://doi.org/10.1109/TIE.2016.2524415).

- [5] Yang Y., Castano S., Yang R., Kasprzak M., Bilgin B., Sathyan A., Dadkhah H., Emadi A., *Design and Comparison of Interior Permanent Magnet Motor Topologies for Traction Applications*, in Transactions on Transportation Electrification, IEEE (2016), DOI: [10.1109/TTE.2016.2614972](https://doi.org/10.1109/TTE.2016.2614972).
- [6] Yu D., Huang X., Fang Y., Zhang J., *Design and comparison of interior permanent magnet synchronous traction motors for high speed railway applications*, in Workshop on Electrical Machines Design, Control and Diagnosis, IEEE (2017), DOI: [10.1109/WEMDCD.2017.7947724](https://doi.org/10.1109/WEMDCD.2017.7947724).
- [7] Chai F., Li Y., Liang P., Pei Y., *Calculation of the Maximum Mechanical Stress on the Rotor of Interior Permanent-Magnet Synchronous Motors*, in Transactions on Industrial Electronics, IEEE (2016), DOI: [10.1109/TIE.2016.2524410](https://doi.org/10.1109/TIE.2016.2524410).
- [8] Du J., Wang X., Lv H., *Optimization of Magnet Shape Based on Efficiency Map of IPMSM for EVs*, in Transactions on Applied Superconductivity, IEEE (2016), DOI: [10.1109/TASC.2016.2594834](https://doi.org/10.1109/TASC.2016.2594834).
- [9] Honda Y., Yokote S., Higaki T., Takeda Y., *Using the halbach magnet array to develop an ultrahigh-speed spindle motor for machine tools*, in Industry Applications Conference 32nd IAS Annual, IEEE (1997), DOI: [10.1109/IAS.1997.643008](https://doi.org/10.1109/IAS.1997.643008).
- [10] Lück P., Bennewitz K., Tausen J., *Volkswagen's electric drivetrains of the new modular e-drive kit (MEB)*, in International VDI Congress, VDI-Berichte Nr. 2354 (2019), DOI: [10.51202/9783181023549-I-515](https://doi.org/10.51202/9783181023549-I-515).
- [11] Huynh T., Chen P., Hsieh M., *Analysis and Comparison of Operational Characteristics of Electric Vehicle Traction Units Combining Two Different Types of Motors*, in Transactions on Vehicular Technology, IEEE (2022), DOI: [10.1109/TVT.2022.3179868](https://doi.org/10.1109/TVT.2022.3179868).
- [12] Hwang Y., Lee J., *HEV Motor Comparison of IPMSM with Nd Sintered Magnet and Heavy Rare-Earth Free Injection Magnet in the Same Size*, in Transactions on Applied Superconductivity, IEEE (2018), DOI: [10.1109/TASC.2018.2807377](https://doi.org/10.1109/TASC.2018.2807377).
- [13] Jiang W., Feng S., Zhang Z., Zhang J., Zhang Z., *Study of Efficiency Characteristics of Interior Permanent Magnet Synchronous Motors*, in Transactions on Magnetics, IEEE (2018), DOI: [10.1109/TMAG.2018.2847328](https://doi.org/10.1109/TMAG.2018.2847328).
- [14] Kato T., Limsuwan N., Yu C., Akatsu K., Lorenz R., *Rare Earth Reduction Using a Novel Variable Magnetomotive Force Flux-Intensified IPM Machine*, in Transactions on Industry Applications, IEEE (2013), DOI: [10.1109/TIA.2013.2283314](https://doi.org/10.1109/TIA.2013.2283314).
- [15] Kim S., Kim Y., Lee G., Hong J., *A Novel Rotor Configuration and Experimental Verification of Interior PM Synchronous Motor for High-Speed Applications*, in Transactions on Magnetics, IEEE (2012), DOI: [10.1109/TMAG.2011.2174045](https://doi.org/10.1109/TMAG.2011.2174045).
- [16] Kim H., Lee C., *Shape Parameters Design for Improving Energy Efficiency of IPM Traction Motor for EV*, in Transactions on Vehicular Technology, IEEE (2021), DOI: [10.1109/TVT.2021.3089576](https://doi.org/10.1109/TVT.2021.3089576).
- [17] Kollmeyer P., McFarland J., Jahns T., *Comparison of class 2a truck electric vehicle drivetrain losses for single- and two-speed gearbox systems with IPM traction machines*, in International Electric Machines & Drives Conference, IEEE (2015), DOI: [10.1109/IEMDC.2015.7409261](https://doi.org/10.1109/IEMDC.2015.7409261).
- [18] Li Y., Liu X., Liu Z., *Analysis and design of an interior permanent magnet synchronous machine with double-layer PMs for electric vehicles based on multi-physics fields*, in International Journal of Computations and Mathematics in Electrical and Electronic Engineering (2018), DOI: [10.1108/COMPEL-09-2016-0425](https://doi.org/10.1108/COMPEL-09-2016-0425).
- [19] Matsuzaki T., Takemoto M., Ogasawara S., Ota S., Oi K., Matsuhashi D., *Operational characteristics of an IPM-type bearingless motor with 2-pole motor windings and 4-pole suspension windings*, in Energy Conversion Congress and Exposition, IEEE (2015), DOI: [10.1109/ECCE.2015.7310209](https://doi.org/10.1109/ECCE.2015.7310209).

- [20] Zhang Z., Liu H., Tengfei Q. S., Zhang Q., *Performance Evaluation of a 60kW IPM Motor for Medium Commercial EV Traction Application*, in Transactions on Electrical Machines and Systems, China Electrotechnical Society (2019), DOI: [10.30941/CESTEMS.2019.00026](https://doi.org/10.30941/CESTEMS.2019.00026).
- [21] Jeong T., Kim W., Kim M., Lee K., Lee J., Han J., Sung T., Kim H., Lee J., *Current Harmonics Loss Analysis of 150-kW Traction Interior Permanent Magnet Synchronous Motor Through Co-Analysis of d-q Axis Current Control and Finite Element Method*, in Transactions on Magnetics, IEEE (2023), DOI: [10.1109/TMAG.2013.2246552](https://doi.org/10.1109/TMAG.2013.2246552).
- [22] Dajaku G., Hofmann H., Hetemi F., Dajaku X., Xie W., Gerling D., *Comparison of Two Different IPM Traction Machines with Concentrated Winding*, in Transactions on Industrial Electronics, IEEE (2016), DOI: [10.1109/TIE.2016.2544720](https://doi.org/10.1109/TIE.2016.2544720).
- [23] Binder A., Schneider T., Klohr M., *Fixation of buried and surface-mounted magnets in high-speed permanent-magnet synchronous machines*, in Transactions on Industry Applications, IEEE (2006), DOI: [10.1109/TIA.2006.876072](https://doi.org/10.1109/TIA.2006.876072).
- [24] Groschup B., Leonardi F., *Combined electromagnetic and static structural simulation to reduce the weight of a permanent magnet machine rotor for HEV application*, in International Electric Machines and Drives Conference, IEEE (2017), DOI: [10.1109/IEMDC.2017.8002194](https://doi.org/10.1109/IEMDC.2017.8002194).
- [25] Lin R., Sudhoff S., Krousgrill C., *Analytical method to compute bridge stresses in V-shape IPMs*, in Electric Power Applications Journal, IET (2018), DOI: [10.1049/iet-epa.2018.0053](https://doi.org/10.1049/iet-epa.2018.0053).
- [26] Polkey W., Pilkey D., *Peterson's stress concentration factors*, John Wiley & Sons (2008).
- [27] Gerlach M., Zajonc M., Ponick B., *Mechanical stress and deformation in the rotors of a high-speed PMSM and IM*, Elektrotechnik und Informationstechnik Journal, OVE (2021), DOI: [10.1007/s00502-021-00866-5](https://doi.org/10.1007/s00502-021-00866-5).
- [28] Mlot A., Korkosz M., Lechowicz A., Podhajecki J., Rawicki S., *Electromagnetic analysis, efficiency map and thermal analysis of an 80-kW IPM motor with distributed and concentrated winding for electric vehicle applications*, in Archives of Electrical Engineering, vol. 71, no. 4, pp. 992–993 (2022), DOI: [10.24425/aee.2022.142120](https://doi.org/10.24425/aee.2022.142120).
- [29] Binder A., *Elektrische Maschinen und Antriebe*, Springer (2012), DOI: [10.1007/978-3-540-71850-5](https://doi.org/10.1007/978-3-540-71850-5).
- [30] Macherauch E., Zoch H.-W., *Praktikum in Werkstoffkunde, 91 ausführliche Versuche aus wichtigen Gebieten der Werkstofftechnik*, Vieweg + Teubner (2011), DOI: [10.1007/978-3-8348-9884-5](https://doi.org/10.1007/978-3-8348-9884-5).
- [31] Kern A., Leuning N., Hameyer K., *Semi-physical demagnetization model for the temperature dependency of permanent magnets in electrical machines*, in AIP Advances (2023), DOI: [10.1063/9.0000400](https://doi.org/10.1063/9.0000400).
- [32] Gerlach M., Zajonc M., Ponick B., *Methodology to Evaluate the Mechanical Stress in High Speed Electric Machines with Buried Magnets*, in International Symposium on Power Electronics, Electrical Drives, Automation and Motion, IEEE (2020), DOI: [10.1109/SPEEDAM48782.2020.9161946](https://doi.org/10.1109/SPEEDAM48782.2020.9161946).